



A generalized wall boundary condition for smoothed particle hydrodynamics

S. Adami ^{*}, X.Y. Hu, N.A. Adams

Institute of Aerodynamics, Technische Universität München, 85748 Garching, Germany

ARTICLE INFO

Article history:

Received 31 May 2011

Received in revised form 13 March 2012

Accepted 5 May 2012

Available online 15 July 2012

Keywords:

Boundary condition

SPH

Solid walls

ABSTRACT

In this paper we present a new formulation of the boundary condition at static and moving solid walls in SPH simulations. Our general approach is both applicable to two and three dimensions and is very simple compared to previous wall boundary formulations. Based on a local force balance between wall and fluid particles we apply a pressure boundary condition on the solid particles to prevent wall penetration. This method can handle sharp corners and complex geometries as is demonstrated with several examples. A validation shows that we recover hydrostatic equilibrium conditions in a static tank, and a comparison of the classical dam break simulation with state-of-the-art results in literature shows good agreement. We simulate various problems such as the flow around a cylinder and the backward facing step at $Re = 100$ to demonstrate the general applicability of this new method.

© 2012 Published by Elsevier Inc.

1. Introduction

Gingold and Monaghan [1] and Lucy [2] presented in 1977, independently from each other, a gridless numerical method to simulate astrophysical problems such as e.g. the fission of a rapidly rotating star. Fundamentally different from gridbased methods, the so-called *smoothed particle hydrodynamics* (SPH) uses a kernel estimation at Lagrangian “grid” points (particles) to solve the governing equations of the system of interest. Moving the particles in time with a flow, pure advection is treated exactly. The rate of change of any conservative variable can be calculated from particle-particle interactions. For this reason SPH has a high potential especially for simulating multi-phase systems and can be applied to a broad variety of problems. Over the past three decades, SPH was successfully used to simulate complex problems ranging from magnetohydrodynamics [3] and solid mechanics [4–7] to fluid mechanics including free surfaces [8,9], surface tension [10,11] and transport phenomena [12,13].

Regardless of the application, boundary conditions are one of the key aspects of a numerical simulation and special attention should be paid to a correct and accurate representation of them. For the example of solid wall boundary conditions, we emphasize the particular importance of a proper formulation of boundary conditions for SPH, as this is crucial to achieve physically meaningful and quantitatively correct results. It is a misconception that SPH models of wall boundary conditions lead to correct results as long as the particle distribution is uniform and stable. Besides preventing particle penetration of the walls, a local force balance is essential to model solid boundaries accurately. We demonstrate the significance of this condition with a numerical freefall experiment in Section 7.1.

Generally, wall models for SPH simulations follow two basic concepts. One concept is to fill the walls with boundary particles to ensure that the support of the smoothing kernel near a wall is completely covered with particles. In the other

* Corresponding author.

E-mail address: stefan.adami@aer.mw.tum.de (S. Adami).

concept, either the non-vanishing surface integral when smoothing the flow quantities close to the boundary is accounted for, or artificial repulsion forces are introduced to prevent that particles cross the interface.

Following the first concept [14], *ghost particles* as mirrors of real fluid particles along the surface are used to fill the solid wall domain. Depending on the velocity assigned to the ghost particle a slip or no-slip condition at the wall can be imposed. Similarly, ghost particles can be used to model symmetry and periodic boundary conditions, but in practice this method is limited to simple interfaces where fluid particles can be mirrored easily at the wall surface. Furthermore, ghost particles have to be created every timestep as mirrors of the evolving fluid particles. Without the need of recreating boundary particles, Morris et al. [15] use fixed wall particles to model curved surfaces and treat them as real particles. The density and the pressure of the boundary particles are evolved in time and they are considered in the continuity equation of the fluid phase. Consequently, the pressure field increases or decreases when particles move towards or away from the wall in order to prevent penetration. When fluid particles interact with boundary particles, the velocity of wall particles is chosen such that either a slip or no-slip condition is satisfied. The calculation of this velocity requires the knowledge of the shape of the wall surface in a closed functional form. Therefore this method cannot directly be applied for arbitrary geometries. Colagrossi [9] use a pointwise mirroring at the local tangent plane of the boundary for arbitrarily shaped walls and impose a free-slip condition at the wall. Density and pressure of these ghost particles are deduced from the fluid phase and the normal velocity component is flipped to ensure no penetration. This method also recreates ghost particles every timestep, and in case of complex geometries special care must be taken to maintain a uniform mass distribution of the ghost particles. Another boundary treatment requiring full support was proposed by Hieber and Koumoutsakos [16], who presented an immersed-boundary method in the context of remeshed smoothed particle hydrodynamics. There, a forcing term is added to the momentum equation such that effectively the no-slip condition is satisfied on a boundary.

The second concept has the advantage that only a single layer of boundary particles at the wall surface is required, i.e. complex geometries are rather easy to handle. DeLeffe et al. [17] account for the fact that the kernel support of fluid particles near walls extends beyond the wall in their so-called normal-flux method by evaluating the non-vanishing surface integral. They show that this method is suitable for testcases with straight walls but do not explain or show how it can be applied to complex geometries. Instead of calculating the surface integral close to the boundary, Ferrand et al. [18] renormalize the smoothing and gradient calculation with respect to the missing kernel support area. But as the geometrical quantities required for the renormalization are evolved in time, this method requires additional computational effort. A very simple technique based on repelling boundary particles is presented by Monaghan et al. [19]. They introduce a Lennard-Jones-like potential between fluid and wall particles to add a repulsion force normal to the boundary. When a fluid particle interacts with a wall particle, only the position of the boundary particle is used to calculate the repulsion force and all other quantities are taken from the fluid phase. But the magnitude of this force has to be calibrated in order to preserve the initial distance between fluid and wall particles on one hand and to prevent penetration on the other hand.

In this work we present a wall boundary formulation that can handle arbitrarily shaped geometries in two and three dimensions. We discretize a solid wall with *dummy* particles and do not evolve their quantities in time. Thus, our approach follows the first of the previously mentioned concepts for modeling solid wall boundaries with SPH. We use the dummy particles to ensure that the support of the kernel interpolants is fully contained within the fluid phase for density change and force calculation. The pressure at a wall particle position for the force calculation is calculated from the surrounding fluid particles with a boundary condition. Including the solid particles in the density change rate calculation ensures a pressure response when fluid particles approach a wall, i.e. the impermeability condition of solid walls is fulfilled. Our formulation is applicable for both stationary and moving walls.

We tested our method with two and threedimensional test cases and found excellent agreement with analytical results and state-of-the-art results in literature. At first, we validate our method with simple straight channel flows such as the Couette and Poiseuille flow. Then, a more complex separated flow past a backward facing step as well as a flow through a periodic lattice of cylinders is simulated, and both compare well with results available in literature. The correctness of our pressure boundary condition is proved with several hydrostatic tank simulations including complex wall geometries, multi-phase problems with different densities and a threedimensional example. A numerical freefall experiment shows the importance of the correct wall boundary formulation including the motion of the wall. We simulate the classical dambreak problem and show very good agreement with state-of-the-art results in literature. Finally, a rotating rippled cylinder simulation demonstrates the coupling of moving walls with complex geometry interacting with a free surface.

2. Governing equations

The governing equations for the motion of an isothermal fluid in a Lagrangian frame of reference are the continuity equation

$$\frac{d\rho}{dt} = -\rho \nabla \cdot \mathbf{v} \quad (1)$$

and the momentum equation

$$\rho \frac{d\mathbf{v}}{dt} = -\nabla p + \mathbf{F}^{(v)} + \rho \mathbf{g} \quad (2)$$

with $\rho, \mathbf{v}, t, p, \mathbf{F}^{(v)}$ and \mathbf{g} denoting the density of a fluid, the velocity, the time, the pressure, the viscous force and a body-force, respectively.

Following the weakly-compressible approach [8,15,20] to simulate incompressible fluids with SPH, an equation of state is introduced to estimate the pressure from the density field via

$$p(\rho) = p_0 \left[\left(\frac{\rho}{\rho_0} \right)^\gamma - 1 \right] + \chi \quad (3)$$

The reference density ρ_0 is set to the initial density of the fluid phase so that the pressure field is initially equal to the background pressure χ . The stiffness of the equation of state can be adjusted with the two parameters p_0 and γ . For fluids it is common to use $\gamma = 7$, and the reference pressure is given by

$$p_0 = \frac{\rho_0 c^2}{\gamma} \quad (4)$$

The artificial sound speed c is chosen based on a scale analysis presented in Morris et al. [15] in order to limit the admissible density variation to 1%. When applied to free-surface flows, the background pressure χ in Eq. (3) is set to zero.

Assuming incompressibility of the fluid, the viscous force $\mathbf{F}^{(v)}$ simplifies to

$$\mathbf{F}^{(v)} = \eta \nabla^2 \mathbf{v} \quad (5)$$

with the dynamic viscosity η .

3. Numerical method

The basic concept of SPH is to advect Lagrangian discretization points with a flow and to interpolate the quantities of these particles from its neighbors with a weighting function W . Generally, any kernel function that satisfies $\int W(\mathbf{r}, h) d\mathbf{r} = 1$ can be used, but due to numerical efficiency it is preferable to require compact support, see Monaghan [21]. Due to a compact kernel support particles which are further away from each other than the cutoff radius r_c do not interact with each other, i.e. $W(|\mathbf{r}| \geq r_c, h) = 0$. The relation of smoothing length h and cutoff radius r_c with $W(r_c = \kappa h) = 0$ is a measure of the smoothing property of the kernel function and the parameter κ varies with the chosen kernel function.

In this work a quintic spline kernel with a compact support of $3h$ is used, i.e. $\kappa = 3$, see Morris et al. [15]. The usage of this kernel is motivated by the work of Hongbin and Xin [22], who showed that the quintic spline or the Gaussian function are favorable for SPH simulations in terms of computational accuracy. Particles are initially placed at Cartesian grid points with a uniform distance Δx to fill the domain. Using Δx as the smoothing length h , in each coordinate direction approximately six particles are spread across the kernel. The volume of a particle V_a is given by $V_a = \Delta x^d$, where d is the number of spatial dimensions. Finally, the mass of each particle is set to $m_a = \rho_a V_a$ and is fixed during the entire simulation. Each particle is tagged with an integer flag to distinguish between fluid particles and solid particles. It is important to create three ($r_c/\Delta x$) layers of dummy particles normal to the wall interface for representing the interface since an accurate integration of the field variables near the interface requires that the support of evolved particles is fully contained within the computational domain.

3.1. Continuity equation

The discretized form of the continuity Eq. (1) for particle a is [21]

$$\frac{d\rho_a}{dt} = \rho_a \sum_b \frac{m_b}{\rho_b} \mathbf{v}_{ab} \cdot \nabla_a W_{ab} \quad (6)$$

where m_b is the mass of particle b , $\mathbf{v}_{ab} = \mathbf{v}_a - \mathbf{v}_b$ is the relative velocity of particle a and b , $\nabla_a W_{ab} = \nabla_a W(\mathbf{r}_a - \mathbf{r}_b, h)$ is the gradient of the weight-function and the summation is performed with all neighboring particles b . Note, that in literature other discretizations of the continuity equation exist [21]. But here we use Eq. (6) since this form holds also for multi-phase problems. The summation over the neighboring particles takes only into account a volume contribution ($m_b/\rho_b = V_b$) and therefore allows a stable simulation even when dealing with high density ratios.

3.2. Momentum equation

According to Hu and Adams [11], the acceleration of particle a due to a pressure gradient can be approximated as

$$\frac{d\mathbf{v}_a}{dt} = -\frac{1}{m_a} \sum_b (V_a^2 + V_b^2) \tilde{p}_{ab} \nabla_a W_{ab} \quad (7)$$

using the density-weighted inter-particle averaged pressure [23]

$$\tilde{p}_{ab} = \frac{\rho_b p_a + \rho_a p_b}{\rho_a + \rho_b} \quad (8)$$

and the volume of both particles V_a and V_b . This form conserves linear and angular momentum exactly as the force between particles a and b is anti-symmetric along the line of centers of the two particles.

The viscous force is derived from the inter-particle-averaged shear stress with a combined viscosity

$$\tilde{\eta}_{ab} = \frac{2\eta_a \eta_b}{\eta_a + \eta_b} \quad (9)$$

For incompressible flows, the acceleration of particle a caused by shear forces simplifies to

$$\frac{d\mathbf{v}_a}{dt} = \frac{1}{m_a} \sum_b \tilde{\eta}_{ab} (V_a^2 + V_b^2) \frac{\mathbf{v}_{ab}}{r_{ab}} \frac{\partial W}{\partial r_{ab}} \quad (10)$$

with $\frac{\partial W}{\partial r_{ab}} = \nabla_a W(\mathbf{r}_a - \mathbf{r}_b, h) \cdot \mathbf{e}_{ab}$ and $r_{ab} = |\mathbf{r}_a - \mathbf{r}_b|$.

Monaghan and Gingold [24] added an artificial viscosity to the momentum equation to stabilize the numerical scheme. Amongst various formulations [21,3] for this dissipative term available in literature, we chose the form

$$\frac{d\mathbf{v}_a}{dt} = - \sum_b m_b \alpha h_{ab} c_{ab} \frac{(\mathbf{v}_a - \mathbf{v}_b) \cdot (\mathbf{r}_a - \mathbf{r}_b)}{\rho_{ab} (|\mathbf{r}_a - \mathbf{r}_b|^2 + \epsilon h_{ab}^2)} \nabla_a W_{ab} \quad (11)$$

as this term can be shown essentially to increase physical viscosity, see Monaghan [25]. The coefficients h_{ab} , c_{ab} and ρ_{ab} are the averages of the smoothing length, the sound speed and the density of the two particles a and b , respectively. The parameter ϵ is usually set to $\epsilon = 0.01$ and is included only to ensure a non-zero denominator. We employ the artificial viscosity to reduce spurious flow oscillations, and therefore it is applied only for interactions between fluid particles, i.e. no artificial dissipation is introduced for the interaction of dummy particles and real particles. The parameter α is chosen such that the global solution is essentially unaffected by the artificial viscosity but also to ensure sufficient damping of spurious oscillations. When using an artificial viscosity in the form of Eq. (11) in the absence of a physical viscosity, an equivalent effective physical kinematic viscosity ν can be calculated from α [26,3] as

$$\nu = \frac{1}{2(d+2)} \alpha h_{ab} c_{ab} \quad (12)$$

In SPH simulations, a jump in initial data causes a transient behavior characterized by spurious high-frequency oscillations due to pseudo-sound waves travelling through the domain. Such artefacts can be reduced by the damping technique proposed by Monaghan et al. [19] during the initial transient of simulations. This damping smoothes the motion of otherwise impulsively accelerated particles. We define a damping time t_{damp} during which the acceleration of each particle due to the body force is mitigated by the factor ζ as follows

$$\zeta(t) = 0.5 \left[\sin \left(\left(-0.5 + \frac{t}{t_{damp}} \right) \pi \right) + 1 \right], \quad t \leq t_{damp} \quad (13)$$

3.3. Time-stepping scheme

The equations of motion are integrated in time with a velocity-Verlet scheme [27]

$$\mathbf{v}_a^{n+\frac{1}{2}} = \mathbf{v}_a^n + \frac{\Delta t}{2} \left(\frac{d\mathbf{v}_a}{dt} \right)^n \quad (14)$$

$$\mathbf{r}_a^{n+\frac{1}{2}} = \mathbf{r}_a^n + \frac{\Delta t}{2} \mathbf{v}_a^{n+\frac{1}{2}} \quad (15)$$

$$\rho^{n+1} = \rho^n + \Delta t \frac{d\rho}{dt}^{n+\frac{1}{2}} \quad (16)$$

$$\mathbf{r}_a^{n+1} = \mathbf{r}_a^{n+\frac{1}{2}} + \frac{\Delta t}{2} \mathbf{v}_a^{n+\frac{1}{2}} \quad (17)$$

$$\mathbf{v}_a^{n+1} = \mathbf{v}_a^{n+\frac{1}{2}} + \frac{\Delta t}{2} \left(\frac{d\mathbf{v}_a}{dt} \right)^{n+1} \quad (18)$$

Although using a mid-point velocity, the force calculation to obtain the particle acceleration has to be performed only once per timestep. In the absence of viscous effects (where the force depends on the velocity) this scheme is second-order accurate and reversible in time.

The step size of the time integration is limited for stability reasons based on several criteria [21]. Here, the three relevant conditions are the CFL-condition based on the artificial sound speed c_{max} and the maximum flow speed

$$\Delta t \leq 0.25 \frac{h}{c_{max} + |\mathbf{v}_{max}|} \quad (19)$$

the viscous condition

$$\Delta t \leq 0.125 \frac{h^2}{\nu} \quad (20)$$

and the body force condition

$$\Delta t \leq 0.25 \left(\frac{h}{|\mathbf{g}|} \right)^{1/2} \quad (21)$$

The minimum of the three conditions is used as timestep to satisfy all conditions globally.

4. Solid wall boundary

Due to the special properties of SPH a whole range of different formulations to impose boundary data is possible. A proper formulation is essential for physically meaningful and quantitatively correct results. As particles approach a rigid boundary, the main problem arises from the fact that the support domain of the kernel is cut by the domain boundary. The question is then how to treat these particles and what boundary conditions have to be imposed. In our method we use dummy particles to approximate the interface between the fluid phase and the boundary, see Fig. 1. The main advantage of dummy particles compared to mirror particles is simplicity when using complex geometries, and that the boundary is well-described throughout the simulation once the particles have been initialized.

In Fig. 1, fluid particles (\bullet) near the wall do interact with dummy particles representing the wall (\circ) according to the overlap of the kernel function. As the governing equations for the flow evolution apply only to the bulk phase wall-particle properties can be manipulated to mimic a continuous fluid phase for particles close to the boundary. Consequently, wall particles represent dummy fluid particles that contribute to the continuity and momentum evolution in the fluid phase. In the continuity equation, Eq. (6), the initial particle volume is used for the wall particles and \mathbf{v}_b is set to the prescribed wall velocity. Thereby the density of a fluid particle increases when moving towards a wall and the resulting pressure force prevents particles from penetrating the walls. Hence, the impermeability condition of rigid walls, i.e. $\mathbf{v} \cdot \mathbf{n} = 0$, is implicitly enforced.

A free-slip or no-slip boundary condition at a wall can be imposed by the choice of the wall velocity used for the viscous interaction in Eq. (10). By simply omitting the viscous interaction of a fluid particle with adjacent dummy particles a free-slip wall boundary condition is applied. To impose a non-slip condition we first extrapolate the smoothed velocity field of the fluid phase to the dummy particle positions by

$$\tilde{\mathbf{v}}_a = \frac{\sum_b \mathbf{v}_b W_{ab}}{\sum_b W_{ab}} \quad (22)$$

Then, the velocity

$$\mathbf{v}_w = 2\mathbf{v}_a - \tilde{\mathbf{v}}_a \quad (23)$$

is assigned to the dummy particle in Eq. (10), where \mathbf{v}_a is the prescribed wall velocity. Compared to the slightly more accurate approach of Morris et al. [15] our method does not require explicit information about the geometry of the boundary, and

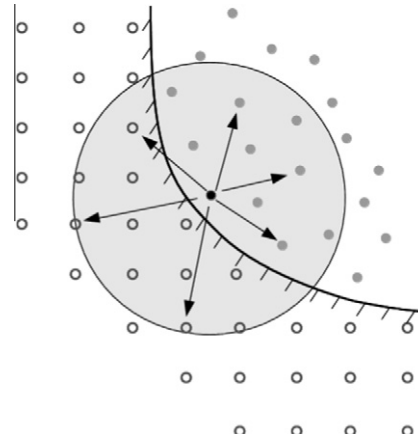


Fig. 1. Fluid particles (\bullet) interact with cartesian dummy particles representing the wall (\circ) to ensure full support of the kernel interpolation.

as the calculation of the extrapolated velocities can be restricted to interface dummy particles the computational overhead is insignificant. Validation simulations for Poiseuille and Couette flows show that we recover the no-slip condition at walls with satisfactory accuracy.

Furthermore, the pressure of a wall particle has to be calculated from the fluid to accurately approximate the pressure gradient in the fluid phase near the boundary. A force balance at the wall interface gives

$$\frac{d\mathbf{v}_f}{dt} = -\frac{\nabla p_f}{\rho_f} + \mathbf{g} = \mathbf{a}_w \quad (24)$$

where the indices f and w refer to the fluid phase and the wall. Note, that here the more general formulation with moving walls is presented. A numerical freefall experiment (Section 7.1) shows that it is important to include the acceleration of the wall \mathbf{a}_w when computing the boundary pressure. From a force balance along the centerline of a fluid-wall particle pair we find

$$\int \nabla p \cdot d\mathbf{l} = \rho_f \int (\mathbf{g} - \mathbf{a}_w) \cdot d\mathbf{l} \quad (25)$$

where $d\mathbf{l}$ is a vectorial length element along the centerline of the two particles and the indices f and w denote a fluid and a wall particle, respectively. The pressure of a wall particle due to the action of a single fluid particle can then be obtained from

$$p_w = p_f + \rho_f(\mathbf{g} - \mathbf{a}_w) \cdot \mathbf{r}_{wf} \quad (26)$$

where $\mathbf{r}_{wf} = r_{wf}\mathbf{e}_{wf}$. Since wall particles interact with several fluid particles, the resulting p_w is obtained by summation of all contributions of neighboring fluid particles f using the kernel function as weight

$$p_w = \frac{\sum_f p_f W_{wf} + (\mathbf{g} - \mathbf{a}_w) \cdot \sum_f \rho_f \mathbf{r}_{wf} W_{wf}}{\sum_f W_{wf}} \quad (27)$$

The calculation of the acceleration of a particle due to a pressure gradient in Eq. (7) uses a density-weighted inter-particle pressure. As we do not evolve the properties of dummy particles in a wall, we obtain its density from the pressure p_w as

$$\rho_w = \rho_{0,b} \left(\frac{p_w - \chi}{p_{0,b}} + 1 \right)^{\frac{1}{\gamma}} \quad (28)$$

from the interacting fluid particle b .

5. Two-dimensional flow examples

The following two-dimensional examples show validation cases to demonstrate the performance of our method. Poiseuille and Couette flow are presented, and very good agreement with exact velocity profiles is found. A correct computation of these flows requires a correct no-slip boundary condition at the walls as the solution depends directly on wall friction. We simulate the laminar flow over a backward facing step at $Re = 100$ to show that separated flows with rectangular walls can be well predicted. The last example, a flow around a cylinder, shows that the method can also handle curved wall boundaries. For all these flows we use a physical friction term in the fluid phase according to Eq. (10) and switch off the additional artificial viscosity term.

5.1. Poiseuille and Couette Flow

Our first examples are a Poiseuille flow and a Couette flow in a two-dimensional infinite channel with a distance between the walls of $L_y = 1$. The fluid phase is discretized with SPH particles at two different resolutions of $r_c = 0.1L_y$ and $0.05L_y$, i.e. 30 and 60 particles across the channel height, respectively. In x -direction we impose periodicity and simulate only a small section of width $L_x = 0.4L_y$. The viscosity and the density of the fluid are $\eta = 0.01$ and $\rho = 1$. The maximum velocity in both cases is $V_{max} = 1.25$, thus we use a sound speed of $c_s = 12.5$ and the Reynolds number of the flows is $Re = 0.0125$. The driving-force of the Poiseuille Flow is a body force $F = 0.1$ and for the Couette flow we move the upper wall with a constant velocity $v_w = 1.25$.

Fig. 2(a) shows a comparison of the SPH simulation with the analytic solution of the Poiseuille flow at $t = 2, 10, 20$ and 100 for two resolutions. Initially, the fluid is at rest and is accelerated by the body-force. At steady-state parabolic velocity profiles have developed and with increasing resolution the simulations converge to the analytical result. The average error of the velocity in flow direction at $t = 10$ for the two resolutions is 0.16% and 0.06%.

A comparison of the SPH simulation with the analytic solution of the Couette flow at $t = 2, 10, 20$ and 100 is shown in Fig. 2(b) for the two resolutions. The simulated profiles agree very well with the analytical results and converge for increasing resolution. Here, the average error of the velocity in flow direction at $t = 10$ for the two resolutions is 0.16% and 0.09%.

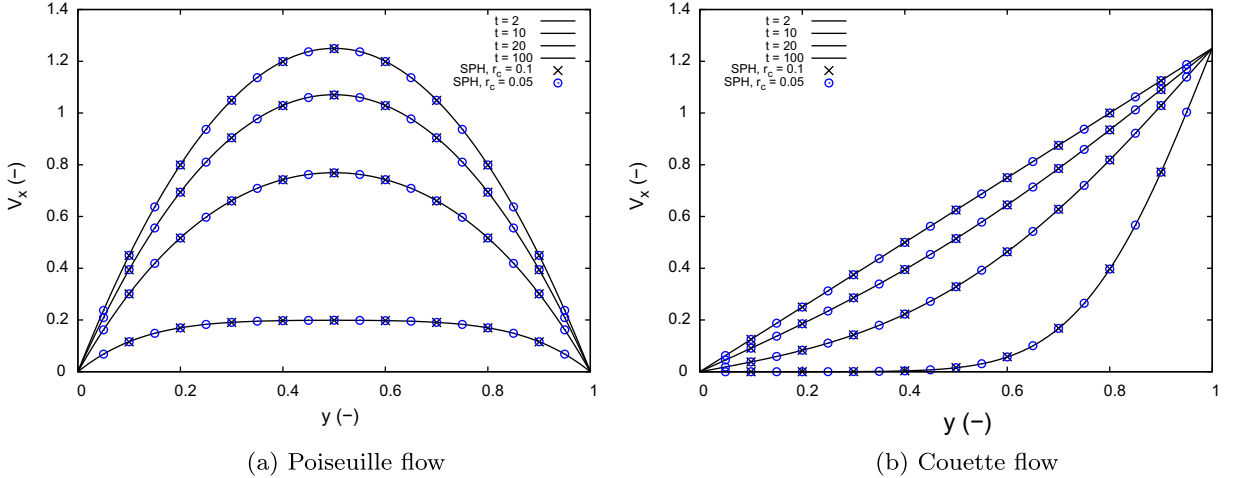


Fig. 2. Comparison of SPH simulations at two resolutions $r_c = 0.1L_y$ and $0.05L_y$ with the analytical solution for the Poiseuille flow (a) and the Couette flow (b).

5.2. Flow over a backward-facing step

We simulate the flow over a backward facing step in a periodic channel at $Re = 100$ and compare our results with the work of Issa et al. [28], who showed that this separated flow can be simulated using SPH. We use the same geometry as presented in [28], see Fig. 3 for a sketch and the dimensions of the problem. The marked positions P_1 – P_4 show the locations where we compare the velocity profiles with the reference results. As there is no analytical solution for this example, the reference solution is obtained from a grid-based high-resolution simulation [29].

Instead of imposing a pressure gradient at the boundaries, we use a constant body force in x -direction to drive the flow in the periodic channel. The magnitude of the body force is adjusted to achieve a mean bulk velocity in the thinner channel above the step of $U = 0.14$. Using twice the channel height above the step as hydraulic diameter $D = 2H_1$, the kinematic viscosity of the fluid $\nu = 1.456 \times 10^{-2}$ follows from $Re = 100$. The sound speed used for this simulations is ten times the maximum velocity in the channel above the step, i.e. $c_s = 2.1$. Also, we have used a small background pressure of $\chi = 0.05p_0$ in the equation of state (3).

The result of the simulation of the flow over the backward-facing step is shown in Fig. 4 for two resolutions $r_c = 0.25$ and $r_c = 0.15$, where $S = 4.9$ is the step height. After an initial transient a steady flow field develops. Fig. 4(a) shows a snapshot at $t = 2000$ of a section of the channel. The fluid particles are colored with the axial velocity ranging from $v_x = -0.015$ (blue) to $v_x = 0.21$ (red). The contour lines are postprocessed after a projection of the particle data onto a Cartesian grid.

When the background pressure in Eq. (3) is omitted, we find large artificial void regions just behind the step similar as presented by Issa [29]. As a remedy, Issa showed that for his method only strongly increasing the speed of sound avoids the particle clumping, leading to a much smaller time step according to the CFL condition. In contrast, we have introduced a small background pressure ($\chi = 0.05p_0$) and maintain a sound speed for $Ma = 0.1$. We find that this constant background pressure is sufficient to prevent void regions in the fluid.

To analyze the quality of the simulation in more detail we plot the streamwise velocity over the channel height at four positions P_1 – P_4 and compare the profiles with the reference results from [29], see Fig. 4(b). The instantaneous particle

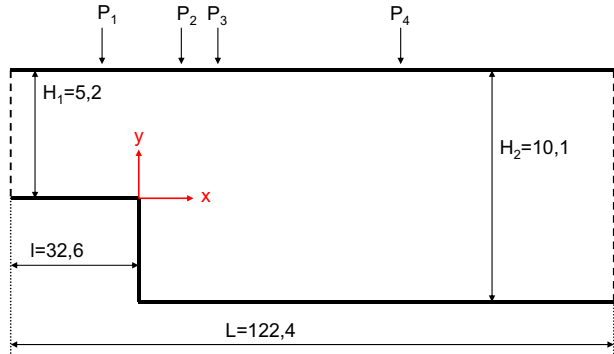
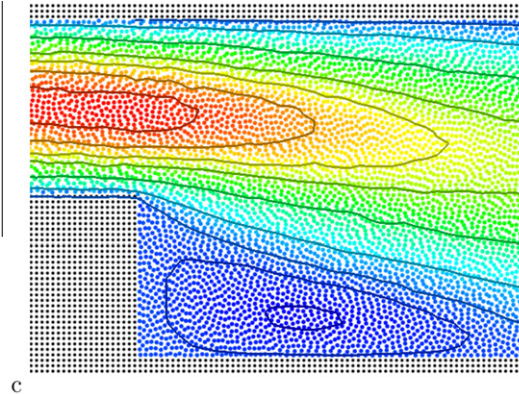
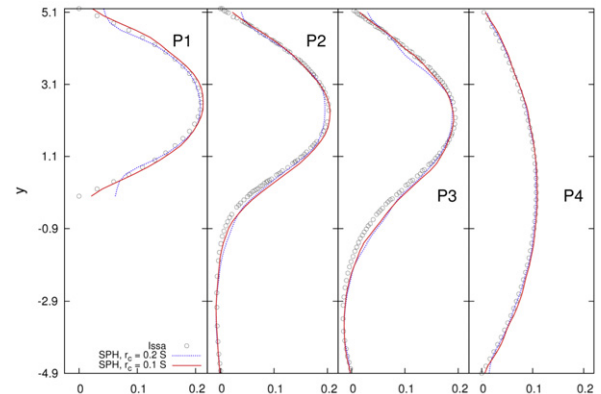


Fig. 3. Sketch of the backward-facing step.



(a) Instantaneous axial velocities at particle positions with contour lines at $t = 2000$, the colormap range is from $v_x = -0.015$ (blue) to $v_x = 0.21$ (red).



(b) Comparison of axial velocity in the channel at positions P_1 - P_4 with reference result for two resolutions $r_c = 0.2 S$ and $r_c = 0.1 S$.

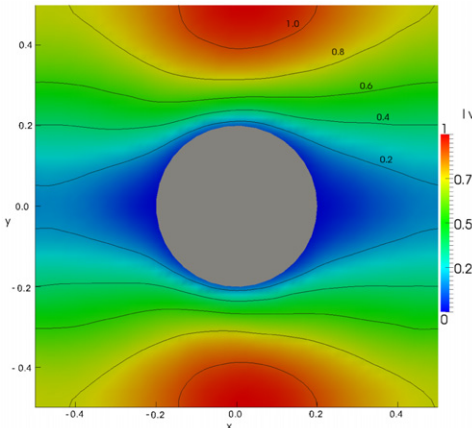
Fig. 4. Simulation results of the laminar flow over a backward-facing step. (For interpretation of the references to colour in this figure legend, the reader is referred to the web version of this article.)

velocities are interpolated on a grid using the kernel W to obtain the smooth profiles. As the profile at P_1 was used to adjust the body force, the agreement with the reference solution at this position is very good. Note, the discrepancy especially for the lower resolution close to the wall is an artefact of the interpolation. The results at P_2 and P_3 show that also the recirculation bubble is well recovered, and in comparison to the SPH results of [28] we match the maximum velocity much better. Far behind the step, the flow field is again parabolic, see P_4 .

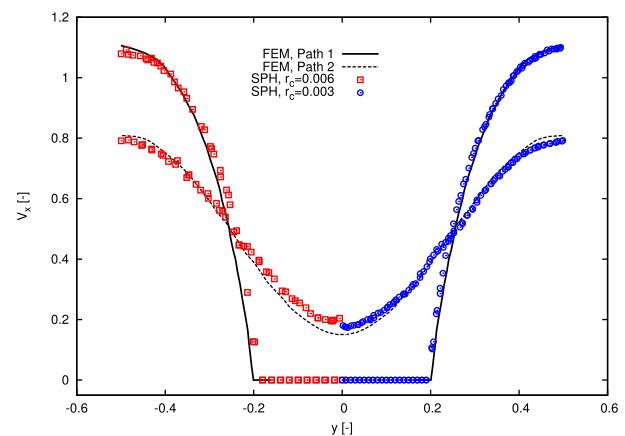
5.3. Flow through a periodic lattice of cylinders

The previous examples have shown the validity of our method for a fluid flow confined by straight channel walls. Now we study the flow through a periodic array of cylinders to test the wall boundary condition for curved geometries. A solid cylinder of radius $R = 0.2$ is centered in a periodic box of size $L = 1$, and the driving pressure gradient for the flow is modeled by a constant body force $F = 1.5$ in x -direction. Following Morris et al. [15] we take the velocity scale to be $V_0 = 0.5$ and a sound speed of $c_s = 5.77$. Using the kinematic viscosity $\nu = 0.1$ in the fluid gives a Reynolds number of $Re = 1$.

The fluid phase is discretized with particles placed initially on a Cartesian lattice at two resolutions using $\Delta x = 0.02$ and $\Delta x = 0.01$. For the cylinder we placed particles on circular rings with the same spacing Δx to increase the smoothness of the solid boundary. This was done for the reason of a better representation of the circular interface compared to using solid particles on a Cartesian lattice at the same resolution. Starting from rest the fluid phase is accelerated by the body force, and after about 5000 steps the particles are completely disordered and a steady flow field has developed. Fig. 5(a) shows the flow



(a) Smoothed velocity field and contour lines for the flow around a cylinder at $Re=1$ using SPH at $\Delta x = 0.02$.



(b) Comparison of SPH and FEM [14] axial velocity profiles at the center of the cylinder and at the domain boundary.

Fig. 5. Simulation results of the flow through a periodic lattice of cylinders.

field and velocity contour lines in the steady state after projecting the particle data onto a Cartesian grid. The velocity magnitude was non-dimensionalized with twice the reference velocity scale $2V_0$. A comparison with the steady incompressible viscous flow using a finite element method (FEM) [15] is shown in Fig. 5(b). The streamwise velocities are plotted over the y -axis at the center of the cylinder and at the downstream domain boundary for particles within a layer of width $2\Delta x$ at these locations. The simulation results agree well with the reference profiles [15], and with increasing resolutions the SPH results converge to the FEM solution.

6. Hydrostatic examples

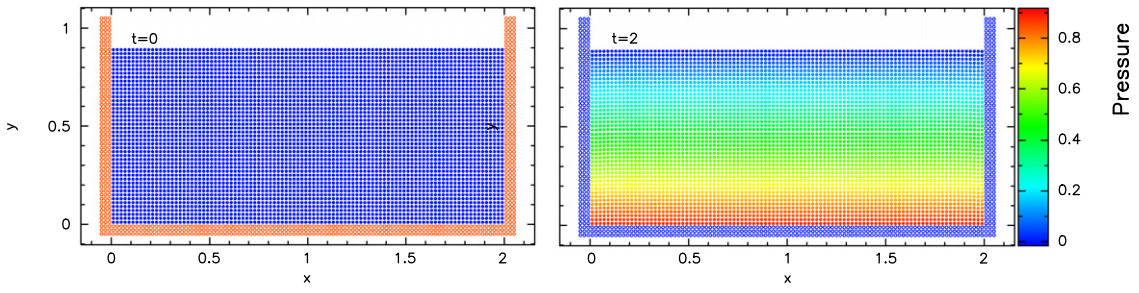
In this section we present several test cases to validate in particular the pressure boundary condition. The first example shows the development of a hydrostatic pressure field of a fluid in a tank under gravity. To show the robustness of our boundary condition we replace subsequently the simple straight wall on one side of the tank by a sharp wedge geometry. Next, the same setup is used to simulate the hydrostatic pressure field in a two-phase configuration where a stratified fluid with two different densities layered on top of each other is considered. Finally, a three-dimensional cylinder example shows the versatility of our method. We use inviscid fluids in all hydrostatic examples, i.e. the physical viscosity is zero. For stabilization of the inviscid flows an artificial viscosity as given by Eq. (11) is necessary.

6.1. Hydrostatic tank

We simulate a two-dimensional cross-section of a rectangular tank with a water depth of $H = 0.9$. The width of the tank is $L_x = 2$ and the walls are about $L_y = 1$ high. Fig. 6(a) shows the initial setup with red particles denoting the wall boundary and blue particles showing the fluid phase. The initial distance between the particles in each direction is $\Delta x = 0.02$, thus a total of 5000 fluid particles is simulated. We chose the sound speed ten times bigger than the reference velocity $v_{ref} = \sqrt{gH}$ and use the artificial viscosity parameter $\alpha = 0.24$. According to Eq. (12) the effective kinematic viscosity corresponds to a Reynolds number of $Re = 100$. Note that we use the same setup as Monaghan et al. [19] in their first example in order to compare the effect of the different boundary condition formulations.

At $t = 0$ the particles are placed on a Cartesian lattice with the density equal to the reference density, thus zero pressure in the fluid phase. Accelerated by the gravity force g in negative y -direction, the particles move down, and due to the compression at the bottom wall their density increases. The pressure response creates a repulsive force, and finally the hydrostatic pressure field counterbalances the body force effect. Thus, after an initial transient phase the particles settle down with a steady and linear pressure field, see Fig. 6(a). We want to highlight the very ordered particle distribution in our simulation compared to previous works [17,19]. We do not see spurious currents in the corners of the tank or a separation of particles from the walls at the free surface. This shows the importance of proper boundary conditions formulated in terms of a force balance as presented in this work.

Fig. 7(a) shows the averaged pressure in the middle of the bottom wall over time, nondimensionalized with $p_{ref} = \rho g H$ and $t_{ref} = H/v_{ref}$. As intended by Monaghan et al. [19] when they introduced the smooth acceleration of particles, the initial damping according to Eq. (13) until $t = 1$ results in a smooth pressure rise and finally the exact value of $p = 1$ is achieved. The pressure profile in the water column is presented in Fig. 7(b). Here, the pressure profile is evaluated along the centerline of the tank by a simple SPH-average $p(y_i) = \sum_j p_j W_{ij} / \sum_j W_{ij}$ using the surrounding fluid particles j . A comparison with the exact linear hydrostatic profile shows very good agreement. Note, the damping technique to smoothly accelerate the particles due to gravity using Eq. (13) mimicks a slowly increasing gravitational acceleration. Thus, to compare the simulated pressure profile during this transient phase the actual gravity used to obtain the analytical hydrostatic profile is also scaled with the factor $\zeta(t)$. At each time instant during the transient period the profile is linear and agrees well with the effective gravitational acceleration.



(a) Initial positions of wall (red) and fluid (blue) particles in the tank. (b) Particle positions at $t = 2$, colored with the pressure field.

Fig. 6. Particle positions (a) and pressure field (b) in the cross-section of a rectangular tank with a water depth of $H = 0.9$ at $t = 0$ and $t = 2$. (For interpretation of the references to colour in this figure legend, the reader is referred to the web version of this article.)

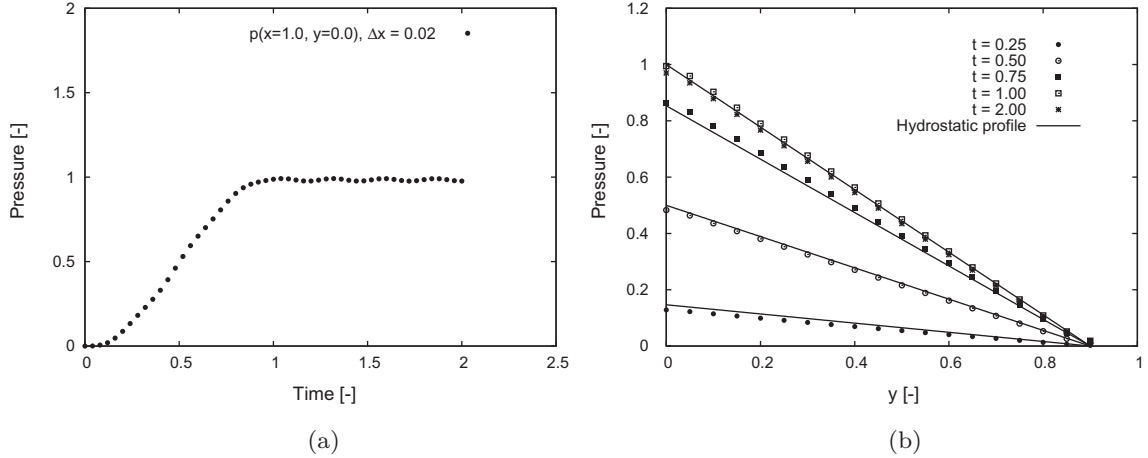


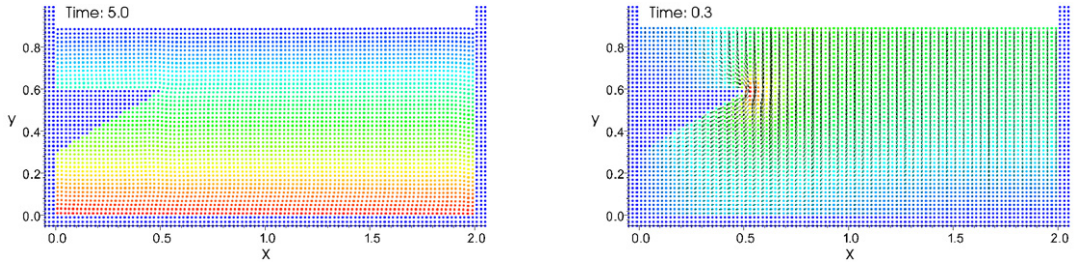
Fig. 7. Temporal (a) and spatial (b) pressure profile at the bottom wall and on the centerline of the hydrostatic tank.

6.2. Hydrostatic tank with complex geometry and two phases

The second example shows the capability of our method to simulate arbitrarily shaped geometries including multi-phase problems. Starting with the geometry of the previously presented cross-section of a watertank, the left wall of the tank is modified with a wedge according to the example presented by DeLeffe et al. [17]. This test demonstrates that even sharp corners in the domain do not cause stability problems and that the correct pressure profile develops in the fluid phase. In Fig. 8(a) the static wall particles are plotted in blue and the fluid particles are colored with the actual pressure at $t = 5$. Again, very good agreement with the analytical hydrostatic pressure profile is achieved and the particles are nearly at rest after the initial transient period.

At $t = 0$ particles are placed on a Cartesian lattice with density equal to the reference density and consequently the pressure is zero in the fluid. Due to the gravitational acceleration the particles move slightly and finally settle down when equilibrium between the external body force and the hydrostatic pressure field is achieved. Fig. 8(b) shows the velocity field in the fluid during the transient phase where particles rearrange under gravity. This snapshot was taken at $t = 0.3$ where the maximum velocity magnitude occurred. The highest velocity magnitude occurs at the sharp corner, but note that it is on the order of only 1% of the reference velocity. At late times, particles are at rest in hydrostatic equilibrium. We compared this result with the results of DeLeffe et al. [17] who simulated this case using a much more complex normal-flux method at the boundaries. They show that the classical ghost particle technique produces a strong circulation zone close to the sharp wedge. Their normal-flux method apparently gives a stationary particle field, but it should be noted that the range of the velocities shown by the colormap in their Fig. 4 about seven times the range we show in Fig. 8(b). In fact, we achieve a very similar result with our rather simple method.

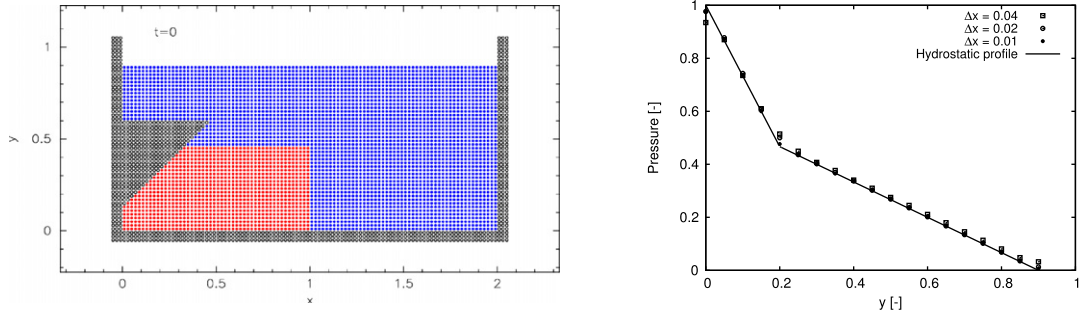
Now we further increase the complexity of this test and introduce a multi-phase problem, where two fluids of different density interact with the walls. Fig. 9(a) shows the initial condition with a resolution of $\Delta x = 0.02$. The heavy phase in the lower left corner ($l_x = 1, l_y = 0.5H$) has a density of $\rho = 1$ and the second fluid is four times lighter ($\rho = 0.25$). Due to gravity, the heavy patch of fluid sloshes against the right wall and displaces the light phase upward. Finally, the two fluids are on top



(a) Fluid particles are colored with the non-dimensionalized pressure, the colormap from blue to red denotes the range of the pressure between zero and one.

(b) This plot shows a snapshot of the velocity field when the velocities are biggest ($t=0.3$). Blue to red color shows the magnitude of the velocity in the range of $0 - 0.015v_{rel}$.

Fig. 8. Pressure field (a) and spurious velocity field (b) for the hydrostatic tank problem with a wedge geometry at $t = 5$ and $t = 0.3$. (For interpretation of the references to colour in this figure legend, the reader is referred to the web version of this article.)



(a) Initial condition for the complex water tank with two phases. Red and blue particles denote the heavy phase with $\rho = 1$ and the light phase with $\rho = 0.25$, respectively. The resolution shown here is $\Delta x = 0.02$.

(b) Non-dimensional pressure profile in the center of the tank compared to piecewise linear analytic profile at $T = 30$.

Fig. 9. Initial condition (a) and final spatial pressure profile (b) in the complex water tank with two phases. (For interpretation of the references to colour in this figure legend, the reader is referred to the web version of this article.)

of each other in hydrostatic equilibrium. Due to the different densities, the pressure gradient in each phase is constant but discontinuous at the interface. The vertical pressure profile in the middle of the tank is plotted in Fig. 9(b) together with the piecewise linear analytical solution. The discrepancy between the exact solution and the numerical results close to the free-surface, the wall and near the phase interface comes from the fact that we used SPH interpolation of the pressure along the vertical line. This smoothes the pressure profile between the heavy and the light phase, and since we only use fluid particles for the interpolation it is obvious that the pressure close to the wall is underestimated, and it is overestimated near the free-surface. With increasing resolution these interpolation effects vanish and the results agree well with the analytical hydrostatic profile. Note that the artificial viscosity parameter α was adjusted for different resolutions following Eq. (12) to maintain a Reynolds number of $Re = 100$.

Several snapshots of the simulation at $t = 2, 4, 6, 8, 10$ and 30 are shown in Fig. 10 for two resolutions of $\Delta x = 0.02$ and $\Delta x = 0.01$. Due to the sloshing of the fluid the interface between the two fluids become distorted, and particles mix. Due to the different densities the phases separate at late times and the fluids settle forming two layers with the heavy phase on the bottom. Additionally, we have added a small constant background pressure to the lighter phase. Similarly to the modification of Colagrossi [9], who changed the pressure equation of state for the light phase, this attempt results in a soft artificial surface tension and suppresses strong mixing of particles of different phases at the interface.

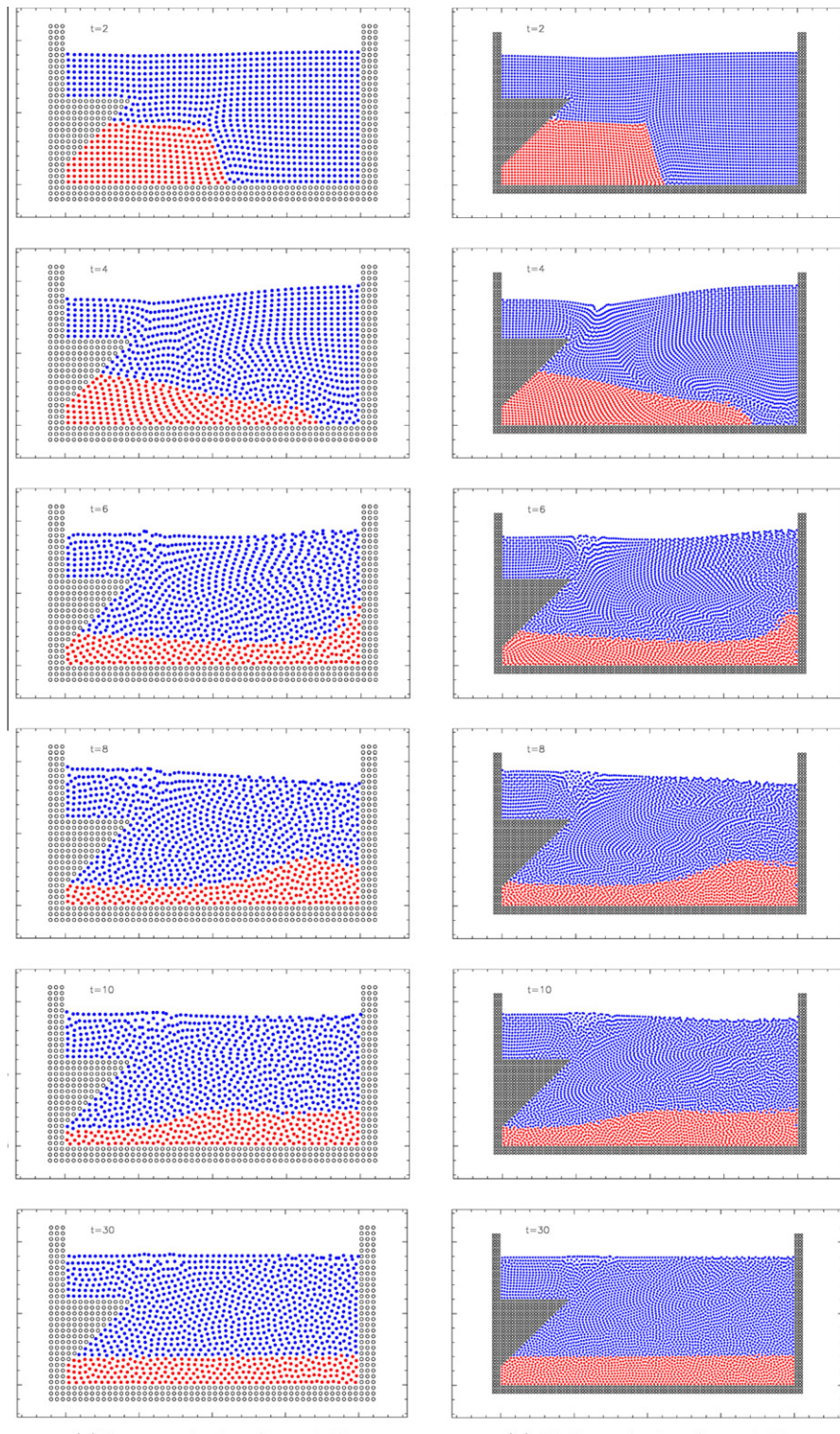
6.3. Threedimensional cylinder

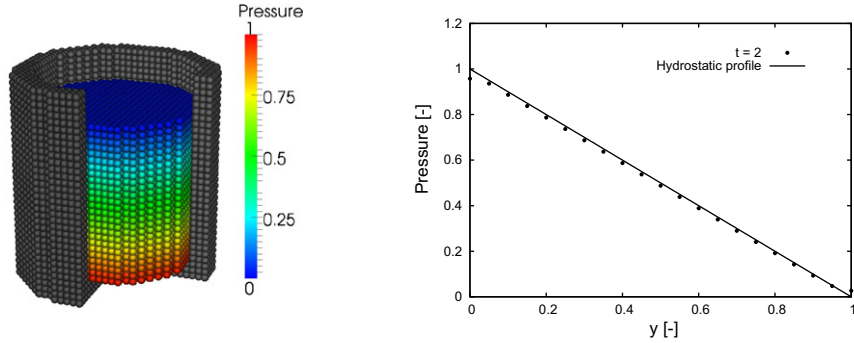
A last hydrostatic example shows the straight-forward application of the proposed method to a threedimensional problem. Now, we simulate a water column of height $H = 1$ in a cylinder with a radius of $R = 0.5$ under gravity. The artificial viscosity in this example is equivalent to a Reynolds number of $Re = 100$. Similar to the previous watertank example we smoothly increase the gravity to avoid strong oscillations in the water. Fig. 11(a) shows a snapshot of the simulation at $T = 2$ with static wall particles in grey and fluid particles colored with the pressure. Note, that the cylinder wall is cut only to visualize the fluid phase.

The reference pressure is $p_{ref} = \rho g H$ and consequently the non-dimensional pressure at the bottom of the cylinder is under hydrostatic equilibrium conditions equal to one, see the colormap in the figure. The pressure profile in the center of the cylinder over the water height is shown in Fig. 11(b). We have interpolated the pressure over the height in the center of the cylinder in z -direction from the particle values. Due to this averaging, the profile is flattened at the free-surface and at the bottom of the cylinder since only fluid particles are included in the summation. This artefact is purely caused by the post-processing and vanishes with increasing resolution. The simulated profile is almost indistinguishable from the analytic linear hydrostatic profile already at the low resolution shown here.

7. Dynamic examples

So far we have only presented simple test cases with stationary walls. Now we want to show the importance of considering the wall motion for the pressure estimation at the wall boundary particles. To the knowledge of the authors this is the first time that such an effect is discussed in terms of the SPH method, and we demonstrate the consequences with a numerical free-fall experiment. Furthermore, we have performed a typical highly dynamical dambreak simulation for which a comparison with results from literature shows good agreement. The final example of a rotating rippled cylinder includes both a quite complex shape and motion of the boundary, demonstrating the robustness and versatility of our method.

(a) Low resolution $\Delta x = 0.02$ (b) High resolution $\Delta x = 0.01$ **Fig. 10.** Snapshots of the two-phase sloshing in a tank with complex wall geometry for different resolutions at $t = 2, 4, 6, 8, 10$ and 30.



(a) Snapshot of the particles at $T = 2$ showing a section of the wall particles (grey) and the fluid particles coloured with the non-dimensional pressure.

(b) Non-dimensional pressure over height in the cylinder compared to the linear analytic profile.

Fig. 11. Hydrostatic water column in a cylinder of radius $R = 0.5$ and water height $H = 1$. Particles are initially placed on cartesian coordinates with $\Delta x = 0.04$.

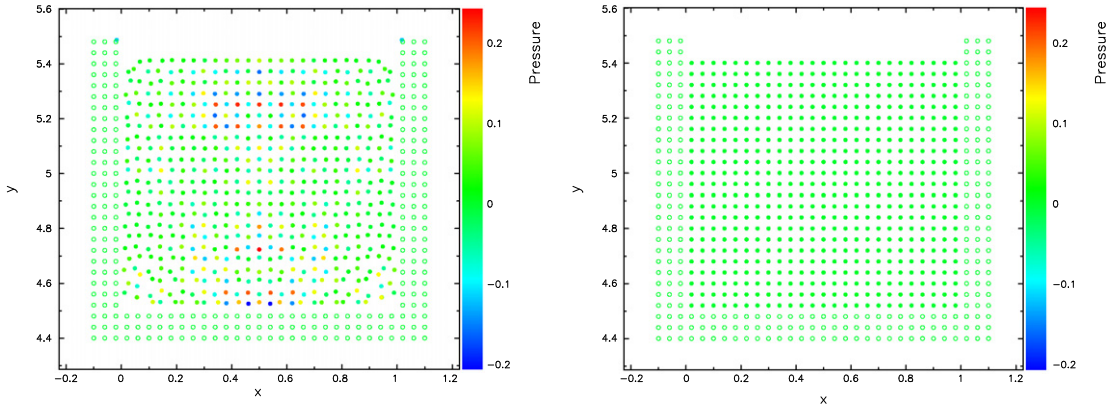
7.1. Freefall experiment

A rectangular two-dimensional tank with water is exposed to a gravity field with a constant acceleration of $g = 1$ in negative y -direction. The water depth in the tank is $H = 0.9$ and the side walls have a length of $L = 1$. We discretize the walls and the fluid phase with initially equidistant particles with $\Delta x = 0.04$ and assign a density of $\rho = 1$ to the water particles. At $T = 0$ the bottom wall is at $y = 5.5$ and due to the body force the tank is accelerated and moving down. Fig. 12 shows two snapshots of the simulation at $T = 1$ where particles are colored with the instantaneous pressure field.

The left snapshot is taken from a simulation where the boundary pressure is not corrected for the acceleration of the wall. That means the pressure in the solid phase contains only the hydrostatic term accounting for the height difference between the fluid and wall particles. Consequently, the pressure of solid particles is non-zero, and fluid particles are pushed off. Finally, fluid particles move relatively to the gravitationally imposed motion, and the noisy pressure field causes a collapse of the simulation. Note also the distortion and non-physical motion especially of the corner particles of the fluid phase in Fig. 12(a). In contrast, Fig. 12(b) shows the same simulation using the full boundary condition as given by Eq. (27). Due to the freefall of the entire body the pressure in the fluid is zero everywhere and particles are at rest relative to the tank motion.

7.2. Dambreak

Now we consider the collapse of a liquid column and compare our results with experimental data and SPH results from literature. First, we study the water-front propagation of a square patch of fluid of size $L = H = 1$ over a dry bed. The fluid



(a) The pressure at boundary particles is calculated from Eq. (27) but neglecting the wall acceleration α_w .

(b) The pressure at boundary particles is calculated from Eq. (27)

Fig. 12. Snapshot of the freefall test example at $T = 1$ for two different boundary particle treatments; particles are colored with local pressure.

phase of density $\rho = 1$ is discretized initially with equidistant particles at cartesian positions with Δx and the artificial viscosity parameter is chosen as $\alpha = 0.4$ to stabilize the simulation. Using $g = 1$ in negative y -direction, all quantities correspond to their non-dimensional variables. Since fluid particles interact with the walls only by the pressure force, the fluid phase is effectively inviscid and slip can occur at the walls. In Fig. 13(a) we monitor the front position of the water column over time in comparison with experimental data taken from Martin and Moyce [30]. At early times the results agree acceptably well, but from about $t > 1$ the simulation clearly overpredicts the speed of propagation of the front position. Due to several uncertainties in this example (effect of surface tension, effect of wall roughness, exact experimental setup) it is not clear what exactly causes the differences, but probably the major difference originates from the fact that the inviscid flow assumption is not appropriate. A rough estimate of the Reynolds number in the experiment gives $Re \approx 400$, thus the inviscid flow assumption at this moderate Reynolds number probably is not yet fully justified. Compared to an analytic water-front velocity derived for inviscid shallow-water conditions by Ritter [31], the simulated front propagation converges to that velocity at late times. We have checked the influence of the artificial viscosity parameter α to ensure that the fluid is unaffected by the numerical dissipation. To show convergence of the results we also have simulated the problem with a higher resolution, see Fig. 13(a). Colagrossi [9] studied the same case using mirror wall particles with free-slip, but imposed initially at $t = 0$ a pressure field in the fluid obtained from a Level-Set method at $t > 0$ to avoid high-frequency oscillations due to acoustic waves in the domain. Not shown here, we have also tested the influence of the initial condition and initialized the water column with a hydrostatic pressure field. As expected, the only difference was a much smaller pressure fluctuation in the fluid since we started the simulation from an equilibrium condition. The water-front propagation was unaffected.

The height of the water column in the simulation and in the experiment is compared in Fig. 13(b). As the velocity of the water-front is overpredicted in the numerical method, the height of the water column over time is slightly lower than in the experiment. The various simulations we have performed give more or less the same evolution of the water height. Again we conclude that the result is independent from the artificial viscosity and from the resolution. Comparing our simulations with results in literature [9,32] we find that our results for the evolution of the water front and height of the water column match with state-of-the-art weakly-compressible SPH simulations with different formulations for wall boundary conditions.

Now we modify the size of the water column and the tank to simulate the classical dam-break problem, as presented in Colagrossi [9]. In this case the water phase covers initially a rectangle of size $L = 2$ and $H = 1$, and the right wall of the tank is positioned at $L_{\text{wall}} = 5.366$. In Fig. 14 we show snapshots of two simulations at different resolution at $T = 1.7, 2.0, 4.8, 5.7, 6.2$ and 7.4. The color of the particles shows the local non-dimensional pressure between $p = 0$ (blue color) and $p = 1$ (red color). The two resolutions used in Fig. 14(k) and (l) are $\Delta x = 0.02$ and $\Delta x = 0.01$. Thus a total of 5000 and 20000 fluid particles was used, respectively. We want to highlight the very good agreement between the two resolutions. The high resolution simulation reproduces the pressure field and free surface of the reference case showing some more small structure, see for example the cavity at the right wall at the free surface at $t = 7.4$.

We compare our results with the simulation of a dam-break flow and impact against a vertical wall by Colagrossi [9]. The free-surface evolution of the breaking column agrees well with the snapshots of [9]. We observe a very similar roll-up and second splash after the impact on the right wall. The main difference is in the pressure field of the fluid. We do not see a pressure distribution similar to a hydrostatic field in the fluid. Our converged results show traveling pressure waves during the highly dynamical collapse of the water column and pressure maxima at the impact positions with the wall. These pressure fluctuations are caused by the weakly-compressible nature of the method, and since viscous effects are small in this case, sound waves are very weakly damped in the simulations. Given the fact that we did not use a smoothed velocity to move the particles (XSPH, [33]) and did not renormalize the density as done in [9], the very good agreement with their results shows that our quite simple method is adequate to handle wall boundaries correctly. We have also confirmed the long-

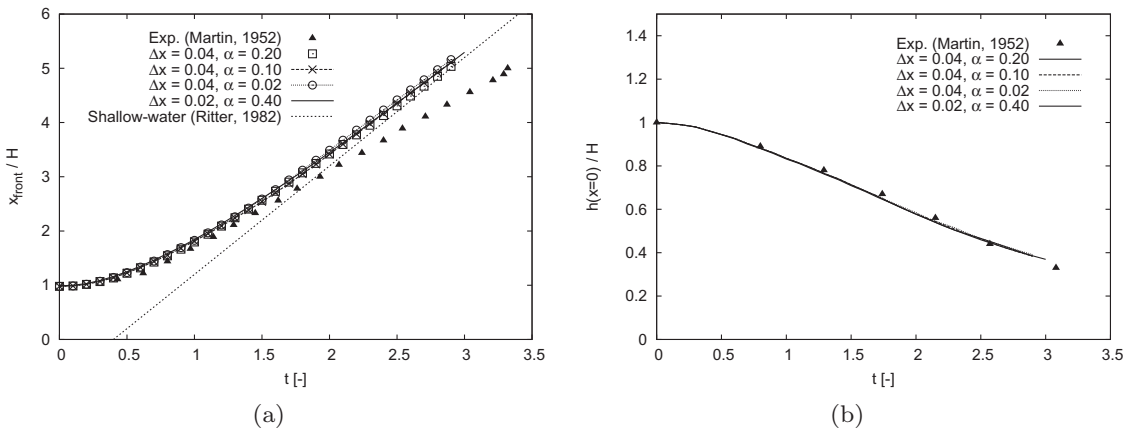
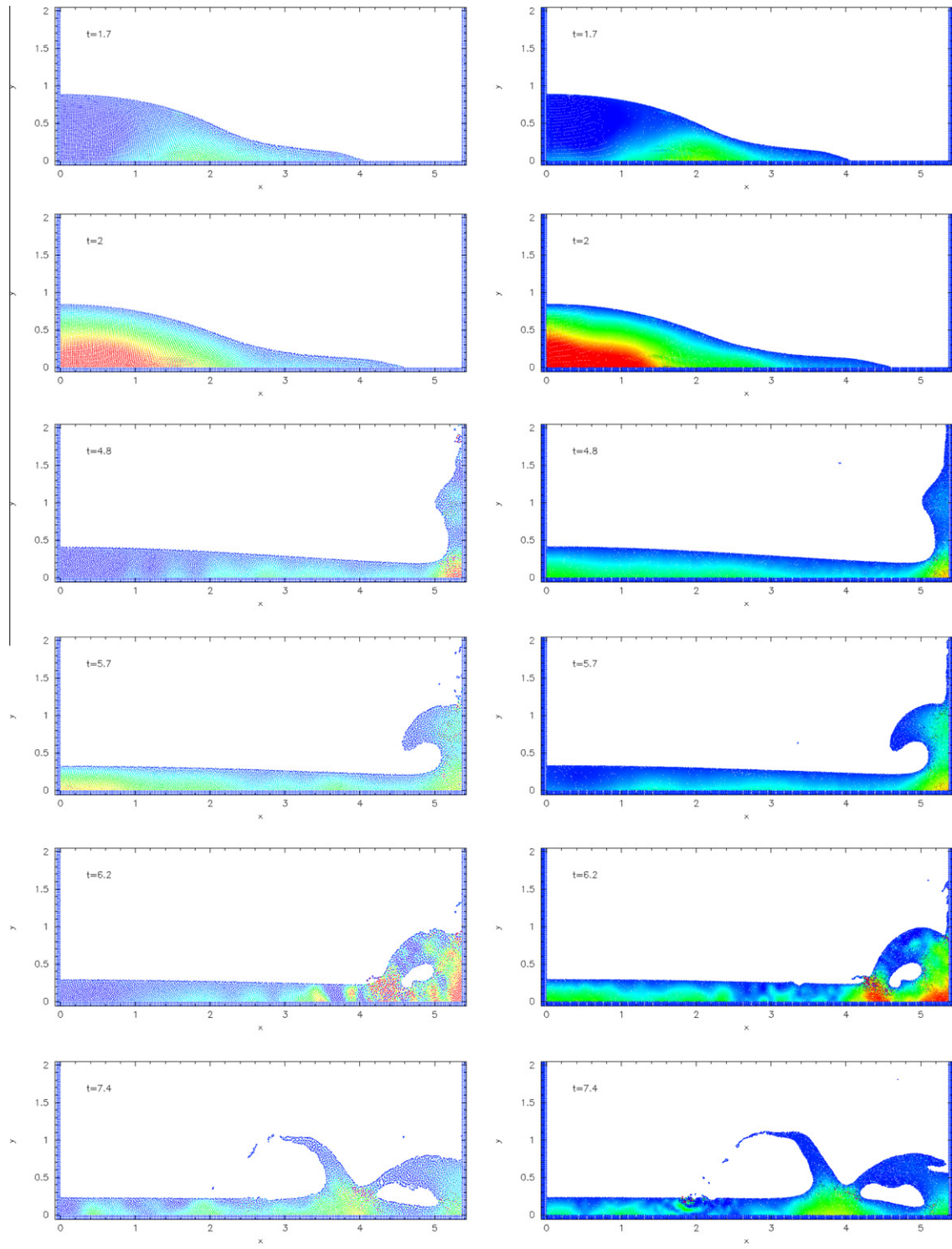


Fig. 13. Time evolution of the front (a) and the height (b) of a collapsing water column for varying parameter of α and Δx compared to experimental data [30].

(k) $\Delta x = 0.02, \alpha = 0.1, 5000$ fluid particles(l) $\Delta x = 0.01, \alpha = 0.2, 20000$ fluid particles**Fig. 14.** Snapshots of the dam-break simulation at $t = 1.7, 2.0, 4.8, 5.7, 6.2$ and 7.4 for two different resolutions.

time stability of our method by simulating six wave impacts at the end walls without facing numerical stability problems, neither for the fluid nor for the boundary particles.

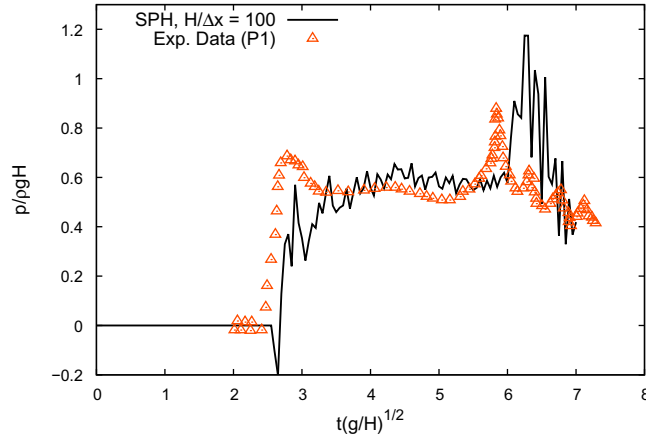


Fig. 15. Comparison of temporal pressure profile at $y/H = 0.2$ between experimental data [34] and SPH simulation with $H/r_c = 100$.

For a quantitative validation we compare the temporal pressure profile on the downstream wall with experimental data from Buchner [34] and the SPH result of Marrone et al. [35]. Fig. 15 shows the pressure on the right wall at $y/H = 0.19$ over time obtained from our simulation and measured data from the experiment [34]. The simulation results were interpolated on this wall position using the same SPH kernel as used in the corresponding calculation. Note, the probe position in the numerical setup does not exactly match the position in the experiment, but Greco [36] showed that this shift gives better agreement and reported several uncertainties in the measurements motivating this adjustment. As expected, the pressure profile obtained with our SPH simulation contains high frequency oscillations but the main pressure plateau is reasonably well captured. The strong peak at $t(g/H)^{1/2} = 6$ is caused by the plunging wave of the first roll-up after the flow hit the wall. As similarly presented already in [35] this peak occurs slightly delayed in the simulation since the air cushion effect is not captured with a mono-fluid simulation.

7.3. Rotating rippled cylinder

Finally, we simulate a cross-section of a partially filled rippled cylinder that is rotating about its own axis. The interface of the cylinder with radius $R = 0.7$ varies with a sinusoidal disturbance with an amplitude of $r_d = 0.1$ and eight periods along the circumference. The height of the water column is $H = 1.0$, measured from the lowest point of the interface. Particles are initially placed on a Cartesian lattice, and the thickness of the wall is equivalent to the cutoff radius r_c , see Fig. 16(a) for a snapshot of the initial setup with $r_c = 0.12$.

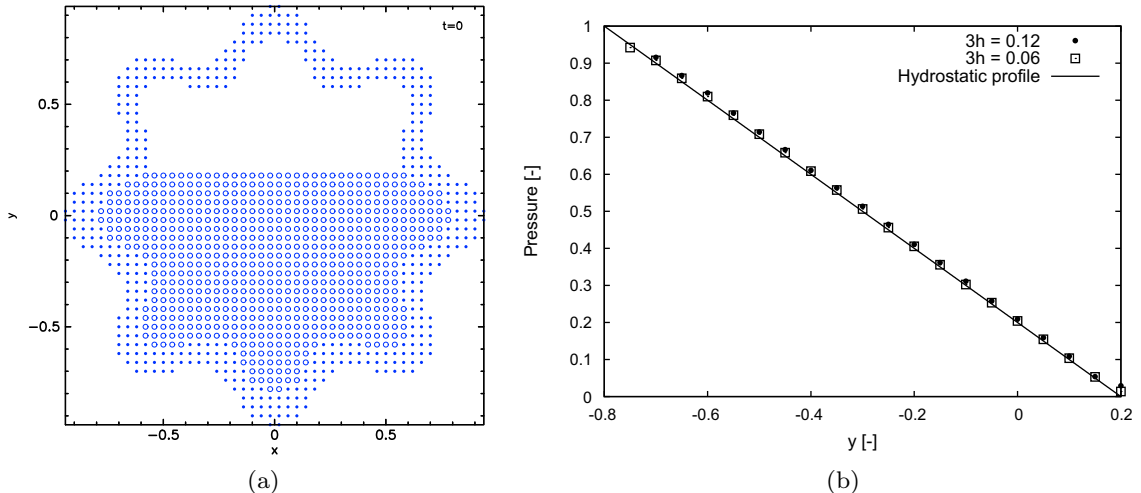


Fig. 16. Rotating rippled cylinder: (a) Initial position of wall (\bullet) and fluid (\circ) particles using a cutoff radius of $r_c = 0.12$. (b) Pressure profile over the height in the center of the cylinder at $T = 18$ for two resolutions $r_c = 0.12$ and $r_c = 0.06$.

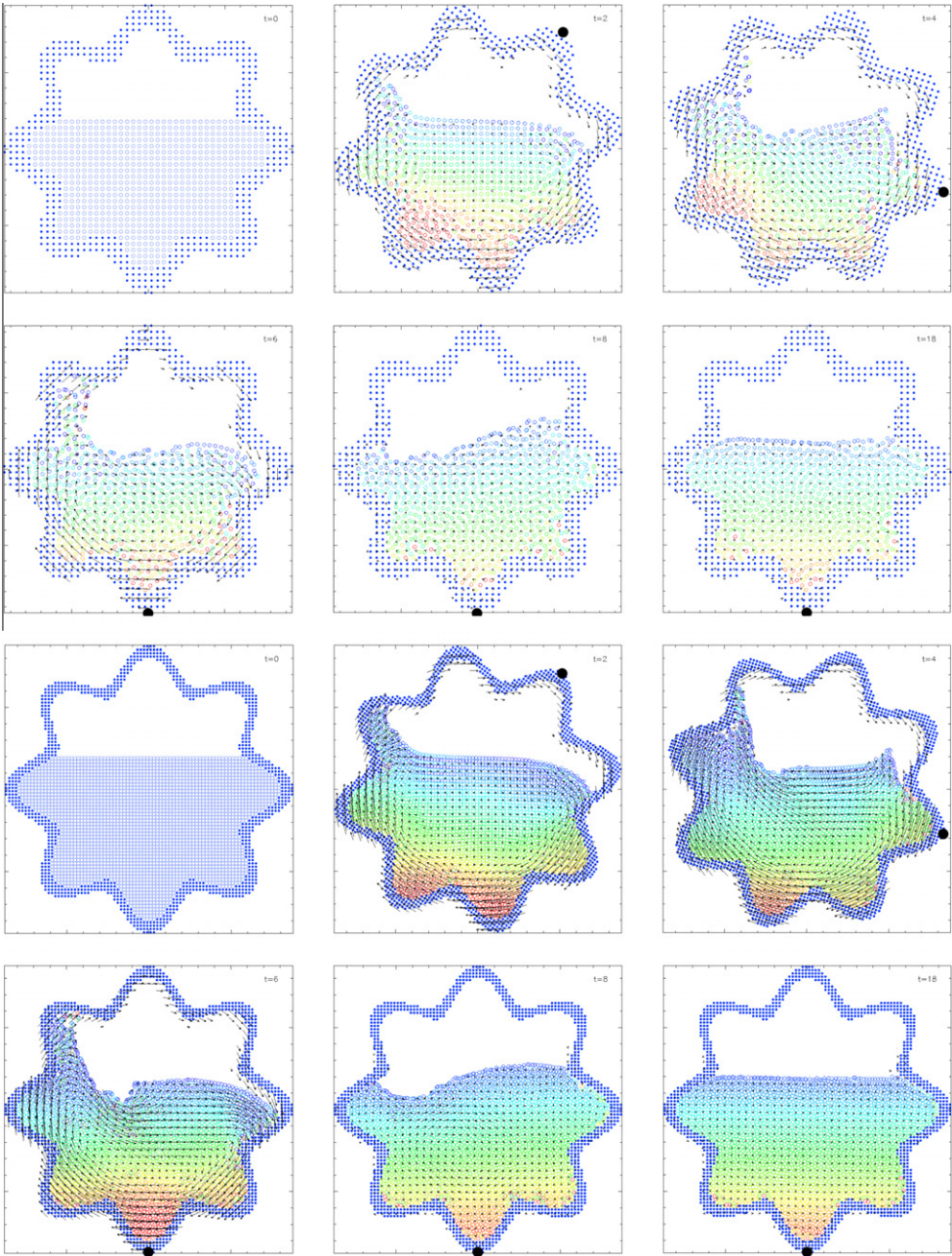


Fig. 17. Snapshots of the rotating cylinder with rippled wall for two resolutions $r_c = 0.12$ (upper half) and $r_c = 0.06$ (lower half). The fluid phase is colored with the pressure field in the range of $p = 0$ (blue) to $p = 1$ (red) and velocity vectors visualize the instantaneous flow field and the rotating cylinder wall. (For interpretation of the references to colour in this figure legend, the reader is referred to the web version of this article.)

First, the water column is exposed to a constant gravitational acceleration of $g = 1$ in negative y -direction. As for the hydrostatic tank simulations, we damp the motion of the fluid until $T = 1$ to smooth spurious oscillations caused by the initial gravitational acceleration. To stabilize the simulation we use a small artificial viscosity $\alpha = 0.1$ which according to Eq. (11) is equivalent to a Reynolds number of $Re = 200$. Then, we rotate the walls with an angular velocity of $\dot{\varphi} = 0.1$ for a half turn. The water column eventually settles in the cylinder with a hydrostatic pressure profile. Fig. 16(b) shows the pressure in the center of the cylinder along the y -axis from the bottom of the wall to the free surface at $T = 18$, where the fluid has settled again after the half turn. The linear slope of the pressure profile in the water column is well reproduced and with increasing resolution the pressure converges to the analytic solution.

A visualization of the flow field and pressure field in the fluid is shown in Fig. 17. The two columns show the result with different resolutions of $r_c = 0.12$ and $r_c = 0.06$ at $T = 2, 4, 6, 8$ and 18 . After the initial damping time $T_{damp} = 1$ the cylinder is rotated with $\dot{\varphi} = 0.1$ until $T = 6$ for a half turn. To clarify the motion of the walls we tracked the initial tip of the cylinder wall with the black bold mark over time in the snapshots. The color in the fluid phase denotes the pressure field in the water in the range of $p = 0$ (blue) to $p = 1$ (red). We also show qualitatively the instantaneous velocity field with velocity vectors. The simulation shows a strong sloshing in the fluid phase due to the rotation of the walls and finally the fluid settles to a hydrostatic water column. With a higher resolution the free surface and flow field reproduce the results of the lower resolution and show some more details of the fluid phase during the sloshing phase. This case demonstrates the robustness of our method for simulating complex moving boundaries interacting with violently moving free-surfaces.

8. Conclusion

We have developed a new approach to simulate solid, non-permeable walls with SPH. Derived from a force balance at the wall boundary, this method incorporates external body forces such as gravitation in dynamical situations. Our proposed boundary particle treatment is simple and general. Solid walls are discretized with dummy particles in a layer of width r_c along the interface. The velocity at dummy particles is extrapolated from the adjacent fluid phase allowing for free-slip or no-slip boundary conditions and a pressure boundary condition prevents penetration of the wall. To calculate the velocity and pressure of dummy particles at the boundary an additional summation over its neighbors has to be performed. But as this operation is limited to interface particles only, i.e. particles that interact with other particles than of its own type/phase, the computational overhead is small. We have shown that our method is capable of simulating hydrostatic problems including complex and sharp wall geometries in two and three dimensions. A numerical freefall experiment demonstrates the relevance of the correct boundary condition for wall particles, and a comparison of the well-known dambreak simulation with results in the literature shows good agreement. The simulation of a rotating rippled cylinder shows that this method is capable of dealing with violent free-surface deformations interacting with moving complex boundaries. Another attractive feature of this wall boundary method is its straightforward extension to fluid–structure-interaction (FSI) problems. Since only geometric information is used, the dummy particles can represent real solid particles or can be evolved according to a separate material law.

Acknowledgments

The authors wish to acknowledge the shared funding of this work by the TUM Graduate School (Technische Universität München) and the German Research Foundation (DFG - Deutsche Forschungsgesellschaft) within the project AD 186/6-1. Computational resources have been provided by the LRZ (Leibniz - Rechenzentrum, computer center for Munich's universities) under Grant pr32ma. We acknowledge the work of Sbalzarini et al. [37] who provided the Parallel Particle Mesh (PPM) Library that we used to implement our model and enables us to perform large-scale simulations on parallel computer architectures. We also gratefully thank Daniel Price (School of Mathematical Sciences, Monash University, Australia) for his introduction and support with *Splash* [38] which was used to produce most of the figures in this paper and John Biddiscombe (CSCS, Swiss National Supercomputing Centre, Switzerland) for his help with *pv-meshless* [39]. Last but not least, sincere thanks go to the reviewers of this paper who ensured that our method is well described.

References

- [1] R. Gingold, J. Monaghan, Smoothed particle hydrodynamics – theory and application to non-spherical stars, *Mon. Not. R. Astron. Soc.* 181 (1977) 375.
- [2] L.B. Lucy, A numerical approach to the testing of the fission hypothesis, *Astron. J.* 82 (12) (1977) 1013.
- [3] D.J. Price, Smoothed particle magnetohydrodynamics – IV. Using the vector potential, *Mon. Not. Roy. Astron. Soc.* 401 (3) (2010) 1475–1499.
- [4] L.D. Libersky, A.G. Petschek, Smooth particle hydrodynamics with strength of materials, in: H. Trease, M. Fritts, W. Crowley (Eds.), *Advances in the Free-Lagrange Method Including Contributions on Adaptive Gridding and the Smooth Particle Hydrodynamics Method*, Lecture Notes in Physics, vol. 395, Springer Berlin Heidelberg, Berlin, Heidelberg, 1991, pp. 248–257.
- [5] W. Benz, E. Asphaug, Simulations of brittle solids using smooth particle hydrodynamics, *Comput. Phys. Commun.* 87 (1–2) (1995) 253–265.
- [6] J. Bonet, S. Kulasegaram, M.X. Rodriguez-Paz, M. Profit, Variational formulation for the smooth particle hydrodynamics (SPH) simulation of fluid and solid problems, *Comput. Methods Appl. Mech. Engrg.* 193 (12–14) (2004) 1245–1256.
- [7] S.E. Hieber, P. Koumoutsakos, A Lagrangian particle method for the simulation of linear and nonlinear elastic models of soft tissue, *J. Comput. Phys.* 227 (21) (2008) 9195–9215.
- [8] J.J. Monaghan, Simulating free surface flows with SPH, *J. Comput. Phys.* 110 (2) (1994) 399–406.
- [9] A. Colagrossi, Numerical simulation of interfacial flows by smoothed particle hydrodynamics, *J. Comput. Phys.* 191 (2) (2003) 448–475.
- [10] J.P. Morris, Simulating surface tension with smoothed particle hydrodynamics, *Int. J. Numer. Methods Fluids* 33 (3) (2000) 333–353.
- [11] X.Y. Hu, N.A. Adams, A multi-phase SPH method for macroscopic and mesoscopic flows, *J. Comput. Phys.* 213 (2) (2006) 844–861.
- [12] A.M. Tartakovsky, P. Meakin, T.D. Scheibe, R. Eichlerwest, R.M.E. West, Simulations of reactive transport and precipitation with smoothed particle hydrodynamics, *J. Comput. Phys.* 222 (2) (2007) 654–672.
- [13] S. Adami, X. Hu, N. Adams, A conservative SPH method for surfactant dynamics, *J. Comput. Phys.* 229 (5) (2010) 1909–1926.
- [14] L.D. Libersky, A.G. Petschek, T.C. Carney, J.R. Hipp, F.A. Allahdadi, High strain lagrangian hydrodynamics, *J. Comput. Phys.* 109 (1) (1993) 67–75.
- [15] J.P. Morris, P.J. Fox, Y. Zhu, Modeling low reynolds number incompressible flows using SPH, *J. Comput. Phys.* 136 (1) (1997) 214–226.
- [16] S. Hieber, P. Koumoutsakos, An immersed boundary method for smoothed particle hydrodynamics of self-propelled swimmers, *J. Comput. Phys.* 227 (19) (2008) 8636–8654.
- [17] M. De Leffe, D. Le Touze, B. Alessandrini, Normal flux method at the boundary for SPH, in: *Proceedings of the 4th SPHERIC Workshop*, 2009, pp. 150–157.

- [18] M. Ferrand, D. Laurence, B. Rogers, D. Violeau, Improved time scheme integration approach for dealing with semi analytic bounday conditions in SPARTACUS2D, in: Proceedings of the 5th SPHERIC Workshop, 2010, pp. 98–105.
- [19] Monaghan, J.J. Monaghan, J.B. Kajtar, SPH particle boundary forces for arbitrary boundaries, *Comput. Phys. Commun.* 180 (10) (2009) 1811–1820.
- [20] L.D.G. Sigalotti, J. Klapp, E. Sira, Y. Melen, A. Hasmy, SPH simulations of time-dependent poiseuille flow at low reynolds numbers, *J. Comput. Phys.* 191 (2) (2003) 622–638.
- [21] J.J. Monaghan, Smoothed particle hydrodynamics, *Ann. Rev. Astron. Astrophys.* 68 (8) (2005) 1703–1759.
- [22] J. Hongbin, D. Xin, On criterions for smoothed particle hydrodynamics kernels in stable field, *J. Comput. Phys.* 202 (2) (2005) 699–709.
- [23] X.Y. Hu, N.A. Adams, An incompressible multi-phase SPH method, *J. Comput. Phys.* 227 (1) (2007) 264–278.
- [24] J.J. Monaghan, R.A. Gingold, Shock simulation by the particle method SPH, *J. Comput. Phys.* 52 (2) (1983) 374–389.
- [25] J.J. Monaghan, Smoothed particle hydrodynamic simulations of shear flow, *Mon. Notices Roy. Astron. Soc.* 365 (1) (2006) 199–213.
- [26] X.Y. Hu, N.a. Adams, Angular-momentum conservative smoothed particle dynamics for incompressible viscous flows, *Phys. Fluids* 18 (10) (2006) 101702.
- [27] L. Verlet, Computer experiments on classical fluids. I. Thermodynamical properties of Lennard–Jones molecules, *Phys. Rev.* 159 (1) (1967) 98.
- [28] R. Issa, E.S. Lee, D. Violeau, D.R. Laurence, Incompressible separated flows simulations with the smoothed particle hydrodynamics gridless method, *Int. J. Numer. Methods Fluids* 47 (10–11) (2005) 1101–1106.
- [29] R. Issa, Numerical assessment of smoothed particle hydrodynamics gridless method for incompressible flows and its extension to turbulent flows, Ph.d. thesis, University of Manchester, 2005.
- [30] J.C. Martin, W.J. Moyce, Part IV. An experimental study of the collapse of liquid columns on a rigid horizontal plane, *Philos. Trans. Roy. Soc. Lond. Ser. A* 244 (882) (1952) 312–324.
- [31] A. Ritter, Die Fortpflanzung der Wasserwellen, *Z. Ver. deut. Ing.* 36 (1982).
- [32] J.P. Hughes, D.I. Graham, Comparison of incompressible and weakly-compressible SPH models for free-surface water flows, *J. Hydraul. Res.* 48 (2010) 105–107.
- [33] J.J. Monaghan, On the problem of penetration in particle methods, *J. Comput. Phys.* 82 (1) (1989) 1–15.
- [34] B. Buchner, Green water on ship-type offshore structures, Ph.D. thesis, Delft University of Technology, 2002.
- [35] S. Marrone, M. Antuono, A. Colagrossi, G. Colicchio, D. Le Touzé, G. Graziani, δ -SPH model for simulating violent impact flows, *Comput. Methods Appl. Mech. Eng.* 200 (13–16) (2011) 1526–1542.
- [36] M. Greco, A two-dimensional study of green-water loading, Ph.D. thesis, 2001.
- [37] I.F. Sbalzarini, J.H. Walther, M. Bergdorf, S.E. Hieber, E.M. Kotsalis, P. Koumoutsakos, PPM A highly efficient parallel particlemesh library for the simulation of continuum systems, *J. Comput. Phys.* 215 (2) (2006) 566–588.
- [38] D.J. Price, SPLASH: An interactive visualisation tool for smoothed particle hydrodynamics simulations, *Publ. Astron. Soc. Aus.* 24 (2007) 159–173.
- [39] J. Biddiscombe, D. Graham, P. Maruzewski, R. Issa, Visualization and analysis of SPH data, *ERCOFTAC Bull.* 76 (2008) 9–12.